

Effect of Co substitution for Fe on microstructure and magnetic properties of FeNiSiBCuNb alloy ribbons

Wen-Feng Liu(刘文峰), Ya-Ting Yuan(袁雅婷), Chang-Jiang Yu(于长江), Shu-Jie Kang(康树杰), Qian-Ke Zhu(朱乾科), Zhe Chen(陈哲), Ke-Wei Zhang(张克维), and Min-Gang Zhang(张敏刚)

Citation: Chin. Phys. B, 2025, 34 (**2**): 027502. DOI: 10.1088/1674-1056/ad9e98
Journal homepage: http://cpb.iphy.ac.cn; http://iopscience.iop.org/cpb

What follows is a list of articles you may be interested in

Electronic structure, elasticity, magnetism of Mn_2XIn(X =Fe, Co) full Heusler compounds under biaxial strain: First-principles calculations

Shiran Gao(皋世苒), Chengyang Zhao(赵成洋), Xinzhuo Zhang(张欣卓), Wen Qiao(乔文), Shiming Yan(颜士明), Ru Bai(白茹), and Tiejun Zhou(周铁军)
Chin. Phys. B, 2025, 34 (**1**): 017501. DOI: 10.1088/1674-1056/ad8ec5

Phase structure evolution and its effect on magnetic and mechanical properties of B-doped Sm_2Co_{17}-type magnets with high Fe content

Yao-Wen Li(李耀文), Zhuang Liu(刘壮), Hai-Chen Wu(吴海辰), Fang Wang(王芳), Chao-Qun Zhu(竺超群), Dong-Liang Tan(谭栋梁), Yu Liu(刘宇), Yang Yang(羊杨), Ming-Xiao Zhang(张明晓), Ren-Jie Chen(陈仁杰), and A-Ru Yan(闫阿儒)
Chin. Phys. B, 2024, 33 (**9**): 097504. DOI: 10.1088/1674-1056/ad5535

Preparation and magnetic hardening of low Ti content $(Sm,Zr)(Fe,Co,Ti)_{12}$ magnets by rapid solidification non-equilibrium method

Xing-Feng Zhang(张兴凤), Li-Bin Liu(刘立斌), Yu-Qing Li(李玉卿), Dong-Tao Zhang(张东涛), Wei-Qiang Liu(刘卫强), and Ming Yue(岳明)
Chin. Phys. B, 2024, 33 (**9**): 097503. DOI: 10.1088/1674-1056/ad58c4

First-principles study of electronic and magnetic properties of Fe atoms on Cu_2N/Cu(100)

Jiale Chen(陈佳乐) and Jun Hu(胡军)
Chin. Phys. B, 2024, 33 (**8**): 087502. DOI: 10.1088/1674-1056/ad5275

Critical behavior of quasi-two-dimensional ferromagnet $Cr_{1.04}Te_2$

Wei Niu(钮伟), Qin-Xin Song(宋沁心), Shi-Qi Chang(常世琦), Min Wang(王敏), Kui Yuan(袁奎), Jia-Cheng Gao(高嘉程), Shuo Wang(王硕), Zhen-Dong Wang(王振东), Kai-Fei Liu(刘凯斐), Ping Liu(刘萍), Yong-Bing Xu(徐永兵), Xiao-Qian Zhang(张晓倩), and Yong Pu(普勇)
Chin. Phys. B, 2024, 33 (**7**): 077506. DOI: 10.1088/1674-1056/ad4cd8

Effect of Co substitution for Fe on microstructure and magnetic properties of FeNiSiBCuNb alloy ribbons

Wen-Feng Liu(刘文峰)[1,2,†], Ya-Ting Yuan(袁雅婷)[1], Chang-Jiang Yu(于长江)[1], Shu-Jie Kang(康树杰)[1], Qian-Ke Zhu(朱乾科)[1,2], Zhe Chen(陈哲)[1,2], Ke-Wei Zhang(张克维)[1,2], and Min-Gang Zhang(张敏刚)[1,2]

[1] *School of Materials Science and Engineering, Taiyuan University of Science and Technology, Taiyuan* 030024, *China*
[2] *Laboratory of Magnetic and Electric Functional Materials and Applications, The Key Laboratory of Shanxi Province, Taiyuan* 030024, *China*

(Received 24 September 2024; revised manuscript received 15 November 2024; accepted manuscript online 13 December 2024)

This work investigated the microstructure, magnetic properties, and crystallization kinetics of the as-spun and annealed alloy ribbons of $(Fe_{40-x}Co_xNi_{40}Si_{6.33}B_{12.66}Cu_1)_{0.97}Nb_{0.03}$, where $x = 0$, 6, 7, 8, 9, prepared using the melt-spinning method. The results show that adding a moderate amount of Co can improve the glass forming ability (GFA), the first peak crystallization temperature, and thermal stability of the as-spun alloy ribbons. With $x = 7$, the two-stage crystallization temperature interval $\Delta T_x = 90$ exhibits optimal thermal stability, and the alloy annealed at 673 K for 10 minutes shows the favorable combined magnetic properties, with $H_c = 0.12$ A/m, $M_s = 88.7$ A·m^2/kg, and $\mu_e = 13800$. The magnetic domain results show that annealing removes numerous pinning points in the magnetic domains of the alloy ribbons, making the domain walls smoother and effectively reducing the pinning effect.

Keywords: amorphous alloys, Co substitution for Fe, glass formation ability, magnetic properties, crystallization kinetics

PACS: 75.60.Nt, 75.60.Ch, 41.20.Gz, 75.50.Kj

DOI: 10.1088/1674-1056/ad9e98 **CSTR:** 32038.14.CPB.ad9e98

1. Introduction

FeNi-based amorphous soft magnetic materials have shown great potential as excellent functional materials in practical applications,[1–3] due to their various excellent properties such as moderate saturation magnetization,[4–6] low coercivity,[7–9] and high magnetic permeability.[10–14] However, there are still many problems that need to be urgently solved, such as low glass forming ability, poor thermal stability, and narrow annealing temperature range. Therefore, it is necessary to develop FeNi-based amorphous alloys with high glass forming ability, good thermal stability, and excellent overall magnetic properties.

To improve the magnetic properties of FeNi-based amorphous alloys, a lot of work have been done. Adjusting the ferromagnetic elements can improve the magnetic properties of FeNi-based amorphous alloys. Gheiratmand *et al.*[15] reported that partial replacement of Fe by Co reduces the amorphous phase magnetostrictive and improves the magnetic properties at higher temperature and frequencies. Sheng *et al.*[16,17] reported that $(Ni_{0.5}Fe_{0.5-x}Co_x)_{80}B_{10}Si_2Cu_1Zr_7$ ($x = 0 \sim 0.5$) alloys show excellent soft magnetic properties with low coercivity (5 A/m∼14 A/m) and high thermal stability. Zhang *et al.*[18] reported that adding a moderate amount of Co improves the glass forming ability by lowering the solid–liquid phase transition temperature and promoting amorphous phase formation. Additionally, heat treatment can further improve the magnetic properties of the alloy. Proper heat treatment can remove residual internal stress and reduce defects in the alloy matrix. However, excessively high annealing temperatures will cause grain crystallization and magnetic anisotropy, which degrades the overall soft magnetic properties. Tong *et al.*[19] investigated the structural origin of magnetic softening in $Fe_{76}Si_9B_{10}P_5$ alloy after annealing. After appropriate annealing, local strengthening of ferromagnetic exchange interaction was achieved, significantly weakens magnetic heterogeneity and obtain excellent soft magnetic properties. The coercivity can be significantly reduced from 25 A/m to 2 A/m. Xi *et al.*[20] studied the effect of annealing on the magnetic properties of $Fe_{86-x}P_{11}C_2B_1Cu_x$ alloy. The results showed that the alloy with $x = 6$ obtained good soft magnetic properties after annealing at 633 K for 10 minutes, with a minimum coercivity value of only 1.2 A/m and a maximum B_s of 1.66 T.

This work investigated the effects of Co partially substitution for Fe on the glass forming ability, thermal stability, and soft magnetic properties of the $(Fe_{40}Ni_{40}Si_{6.33}B_{12.66}Cu_1)_{97}Nb_3$ amorphous alloy. Meanwhile, the effects of annealing conditions on the comprehensive magnetic properties, structure, and crystallization dynamics of the alloys are also studied. The aim is to improve the soft magnetic properties of the alloy, identify optimal annealing processes, and provide a theoretical basis for developing high-performance FeNi-based amorphous alloys.

[†]Corresponding author. E-mail: wfliu@tyust.edu.cn

© 2025 Chinese Physical Society and IOP Publishing Ltd. All rights, including for text and data mining, AI training, and similar technologies, are reserved.

2. Experimental procedure

2.1. Preparation of FeNi-based amorphous alloys

High purity elements (Fe: 99.99 at.%, Co: 99.99 at.%, Ni: 99.99 at.%, Si: 99.99 at.%, B: 99.99 at.%, Cu: 99.99 at.%, Nb: 99.99 at.%, Mb: 99.97 at.%) were mixed in a specific ratio using a vacuum induction melting furnace under an argon atmosphere. The master alloy ingot, with the composition $(Fe_{40-x}Co_xNi_{40}Si_{6.33}B_{12.66}Cu_1)_{0.97}Nb_{0.03}$ ($x = 0$, 6, 7, 8, 9) was prepared by mixing and melting 3–4 times to ensure uniform composition. Then, the alloy was cast into thin ribbons, approximately 2-mm wide and 23-μm thick, using a standard procedure of rapid quenching of the melt on a rotating disc (melt-spinning method) with a surface speed of 28.6 m/s. The ribbons were annealed in muffle furnaces with argon-filled quartz tubes at various temperatures and time, with a constant heating rate of 5 K/min.

2.2. Characterization

The structure of the as-spun and annealed alloy ribbons was analyzed by a miniature x-ray diffractometer (XRD, DX-27) with Cu $K\alpha$ radiation ($\lambda = 1.5418$ Å). Thermal analysis was performed with a differential scanning calorimeter (DSC, NETZSCH STA 449F3), in which the protective gas was argon, and the heating rates from room temperature to 1100 K with 10 K/min, 20 K/min, 30 K/min, and 40 K/min, respectively, and the test method was a non-isothermal test. Magnetization strength (M_s) and coercivity (H_c) were measured using a vibrating sample magnetometer (VSM, Versalab) and a DC soft magnetic measuring device (MATS-2010SD), while an impedance analyzer (Agilent 4294A) was used to determine the effective permeability (μ_e).

3. Results and discussion

3.1. Amorphous formation capability and thermal stability

Figure 1 shows the XRD patterns of the as-spun $(Fe_{40-x}Co_xNi_{40}Si_{6.33}B_{12.66}Cu_1)_{0.97}Nb_{0.03}$ ($x = 0$, 6, 7, 8, 9) alloy ribbons. The patterns exhibit only a typical broad scattering peak at $2\theta \approx 45°$, indicating the amorphous structure of the as-spun alloy ribbons.

Figure 2(a) shows the hysteresis loop of the as-spun $(Fe_{40-x}Co_xNi_{40}Si_{6.33}B_{12.66}Cu_1)_{0.97}Nb_{0.03}$ ($x = 0$, 6, 7, 8, 9) alloy ribbons. Figure 2(b) presents the variation in saturation magnetization (M_s) and coercivity (H_c) of the alloy ribbons with different Co contents. The M_s increases initially and then decreases with rising Co content, peaking at 94.9 A·m^2/kg with $x = 6$. The initial increase of M_s is likely due to the improved ferromagnetic exchange caused by Co substitution for Fe. However, beyond this optimal Co content, M_s declines because of Co atoms, having a lower magnetic moment than Fe atoms, reduce the overall magnetic moment when their concentration is increased. Therefore, the M_s decreases. The H_c first decreases and then increases, reaching a minimum of 7.2 A/m with $x = 7$. The initial decrease in H_c is attributed to improved amorphous formation and a more homogeneous structure with fewer grain boundaries and less component segregation, facilitating easier magnetic moment movement. However, excessive Co will increase the anisotropy of the alloy and increase the H_c.

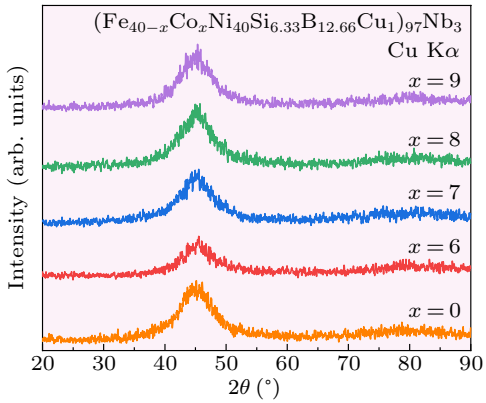


Fig. 1. XRD patterns of as-spun $(Fe_{40-x}Ni_{40}Co_xSi_{6.33}B_{12.66}Cu_1)_{0.97}$ $Nb_{0.03}$ ($x = 0$, 6, 7, 8, 9) alloy ribbons.

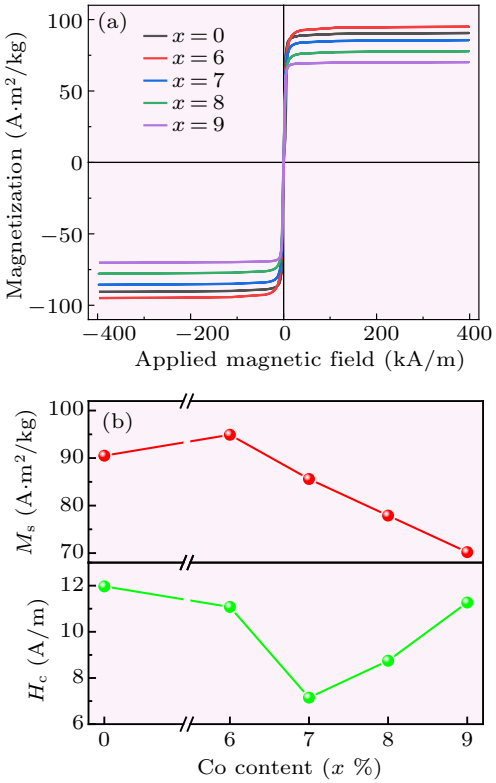


Fig. 2. (a) Hysteresis loop of the as-spun $(Fe_{40-x}Co_xNi_{40}Si_{6.33}B_{12.66}$ $Cu_1)_{97}Nb_3$ ($x = 0$, 6, 7, 8, 9) alloy ribbons and (b) variation in saturation magnetization (M_s) and coercivity (H_c) of the alloy ribbons.

Figure 3 presents the DSC curves of the as-spun $(Fe_{40-x}Co_xNi_{40}Si_{6.33}B_{12.66}Cu_1)_{0.97}Nb_{0.03}$ ($x = 0$, 6, 7, 8, 9) alloy ribbons. All alloys exhibit three exothermic peaks during crystallization, indicating the presence of multiple crystallization processes. Figure 4 presents the T_x and ΔT_x curves

for the $(Fe_{40-x}Co_xNi_{40}Si_{6.33}B_{12.66}Cu_1)_{0.97}Nb_{0.03}$ ($x = 0$, 6, 7, 8, 9) alloy ribbons. The data show that adding Co increases both T_{x1} and T_{x2} compared to the alloy without Co. This indicates that moderate Co addition improves the first crystallization temperature and the glass forming ability of the alloy, thereby improving the thermal stability. At $x = 7$, the curve shows the highest two-stage onset crystallization temperatures and the largest two-stage crystallization temperature interval (ΔT_x), demonstrating the best glass forming ability (GFA) and thermal stability. The results suggest that Co addition promotes the formation of a high-density atomic structure, which increases the solid–liquid interfacial energy and the viscosity of the supercooled liquid. This effectively hinders atomic movement during crystallization or solidification, enhancing the stability of the supercooled liquid and the glass forming ability of the alloys.

The amorphous state is thermodynamically a substable structure that absorbs energy when heated and transforms into a steady-state crystalline structure. The crystallization process of the amorphous alloy is closely related to its crystallization temperatures. Typically, the glass forming ability and thermal stability are assessed by analyzing the DSC curves, focusing on the onset crystallization temperature (T_x) and the peak crystallization temperature (T_p). A higher T_x shows the greater difficulty in nucleation, while a higher T_p suggests that crystal growth is more challenging.[21] Crystallization analysis methods are generally categorized into non-isothermal and isothermal approaches.[22]

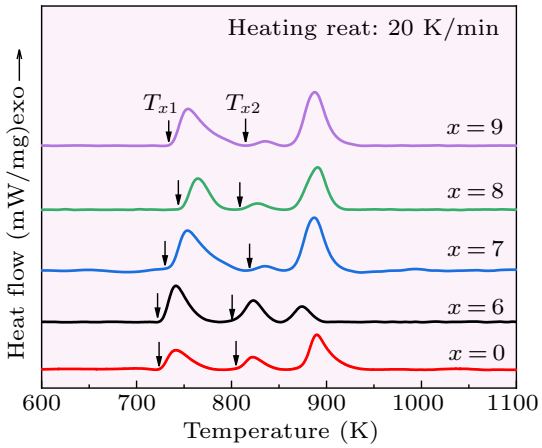


Fig. 3. DSC curves of $(Fe_{40-x}Co_xNi_{40}Si_{6.33}B_{12.66}Cu_1)_{97}Nb_3$ ($x = 0$, 6, 7, 8, 9) alloy ribbons.

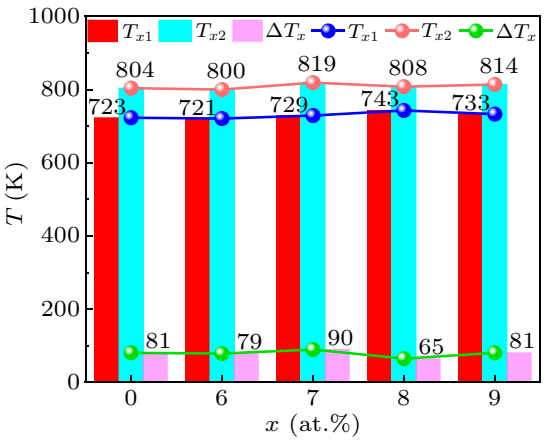


Fig. 4. The T_x and ΔT_x curves of $(Fe_{40-x}Co_xNi_{40}Si_{6.33}B_{12.66}Cu_1)_{97}Nb_3$ ($x = 0$, 6, 7, 8, 9) alloy ribbons.

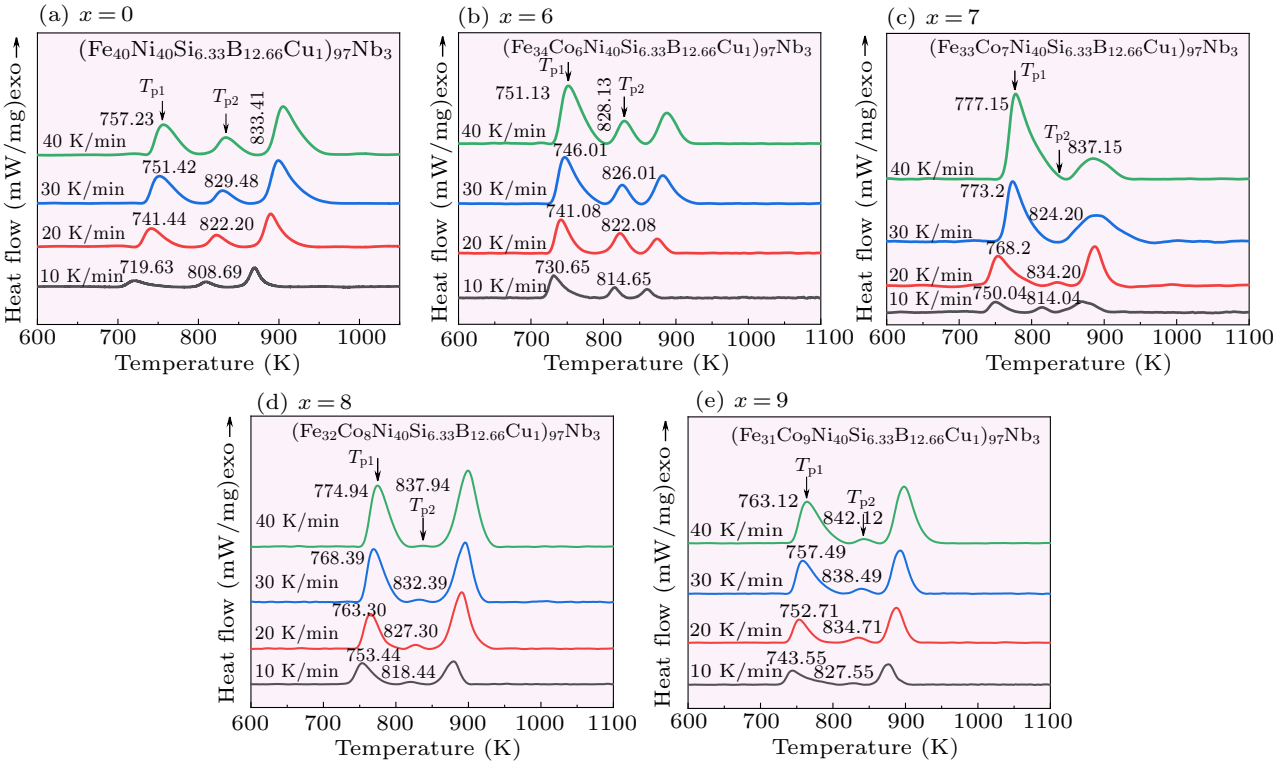


Fig. 5. DSC curves at room temperature of as-spun $(Fe_{40-x}Co_xNi_{40}Si_{6.33}B_{12.66}Cu_1)_{97}Nb_3$ ($x = 0$, 6, 7, 8, 9) alloy ribbons at different heating rates: (a) $x = 0$, (b) $x = 6$, (c) $x = 7$, (d) $x = 8$, and (e) $x = 9$.

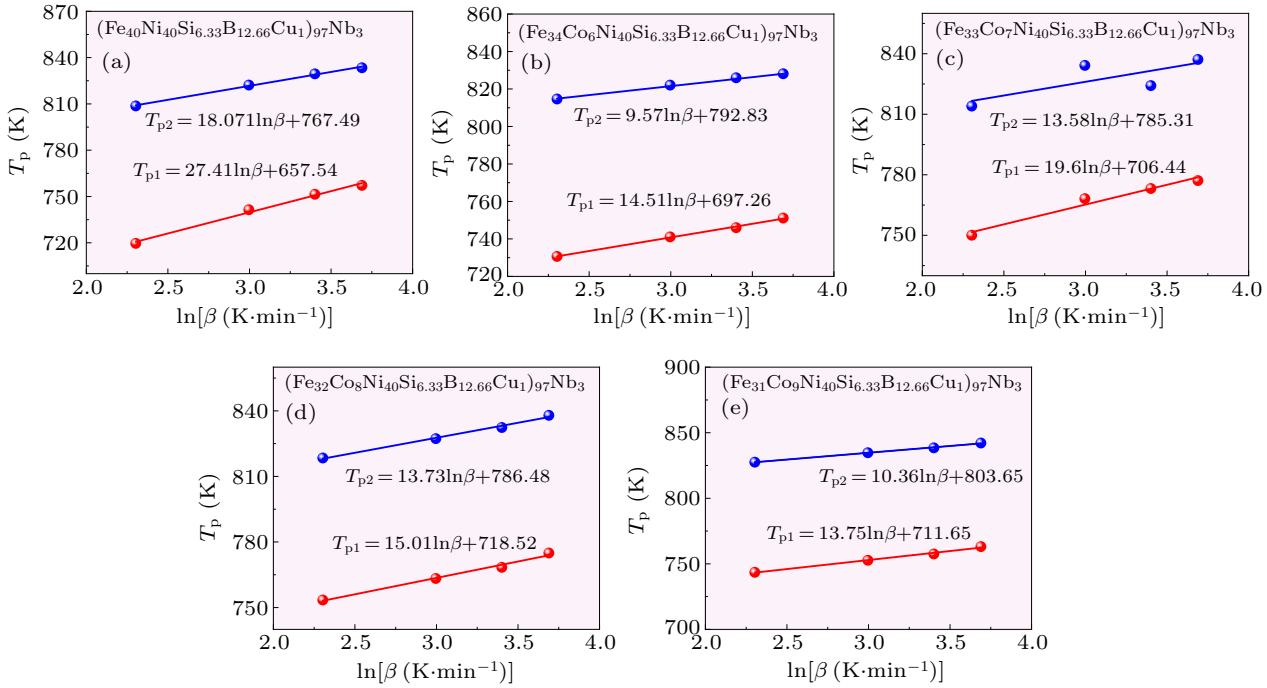


Fig. 6. The relation between T_p and $\ln\beta$ of $(Fe_{40-x}Co_xNi_{40}Si_{6.33}B_{12.66}Cu_1)_{97}Nb_3$ ($x = 0$, 6, 7, 8, 9) alloy ribbons for (a) $x = 0$, (b) $x = 6$, (c) $x = 7$, (d) $x = 8$, and (e) $x = 9$.

In this study, a fast and methodologically convenient non-isothermal analytical method was used. Figure 5 shows the non-isothermal DSC curves of the as-spun $(Fe_{40-x}Co_xNi_{40}Si_{6.33}B_{12.66}Cu_1)_{97}Nb_3$ ($x = 0$, 6, 7, 8, 9) alloy ribbons at heating rates of 10 K/min, 20 K/min, 30 K/min, and 40 K/min. The data shows that higher heating rates result in higher crystallization peak temperatures, demonstrating a clear kinetic effect. Crystallization nucleation is closely related to the annealing process. During slow heating, atoms have sufficient time to absorb energy, diffuse, and rearrange, leading to a shorter crystallization time. In contrast, during rapid heating, the reduced time for these processes requires a higher temperature to provide the necessary energy for nucleation and growth. Therefore, as the heating rate increases, the temperature of the crystallization peak also rises.

Crystallization behavior in amorphous alloys depends on the heating temperature, and changes in the peak crystallization temperature with heating rate and reflect the thermal stability of the crystallization process. To analyze how the crystallization peak temperature is affected by the heating rate, figure 6 presents the fitted curves of the two crystallization peak temperatures *versus* $\ln\beta$ for $(Fe_{40-x}Co_xNi_{40}Si_{6.33}B_{12.66}Cu_1)_{97}Nb_3$ ($x = 0$, 6, 7, 8, 9) alloy ribbons. The relationship between T_p and $\ln\beta$ for these alloys can be described using Lasocka's equation[23]

$$T_p = A + B\ln\beta. \tag{1}$$

In this equation, T_p represents the crystallization peak temperature, β is the heating rate, and A and B are constants. The constant A denotes the characteristic temperature at a heating rate of 1 K/min, while B shows the sensitivity of T_p to β, with higher values of B reflecting greater sensitivity. As shown in Fig. 6, both the first peak crystallization temperature (T_{p1}) and the second peak crystallization temperature (T_{p2}) of all alloys show a good linear correlation with $\ln\beta$. Figure 7 shows the variation of B_1 and B_2 with different Co contents. It is evident that both B_1 and B_2 initially increase and then decrease with increasing Co content, with B_1 reaching its maximum at 7 at.% Co. The initial increase occurs because of Co, having a smaller atomic radius than Fe, reduces the barriers to atomic movement when it replaces Fe. This reduction facilitates more rapid atomic diffusion and rearrangement during heating, thereby increasing the crystallization nucleation rate and making the crystallization peak temperature more sensitive to the heating rate. The decrease in B_1 is attributed to the presence of γ-(Fe,Ni,Co) clusters, which, once crystallized and grown to a larger size, lead to a reduced nucleation rate and thus a lower B_1 value. The B_2 value first increases and then decreases, peaking at 8 at.% Co. The initial increase is due to the primary phase providing nucleation sites for the second crystalline phase, facilitating its precipitation and causing a slight increase in B_2. However, B_2 then decreases as the number of nucleation sites becomes saturated, reducing the rate of nucleation for the second phase.

Crystallization activation energy represents the energy barrier that must be overcome for an amorphous alloy to transform into a crystalline structure. A higher activation energy shows greater difficulty in crystallizing the amorphous alloy and higher thermal stability.[23–26] This energy can be deter-

mined using the Kissinger formula, given as follows:[27]

$$\ln(\beta/T^2) = -E/RT + C, \tag{2}$$

where E denotes the crystallization activation energy, T is the characteristic temperature, R is the ideal gas constant (8.314 J·mol^{-1}·K^{-1}), and C is a constant. The crystallization activation energy was determined by curveting $\ln(\beta/T_p)$ against $1000/T_p$ for various heating rates and crystallization peak temperatures, followed by linear fitting as shown in Fig. 8. The activation energy is obtained by multiplying the slope of the fitted line by R.

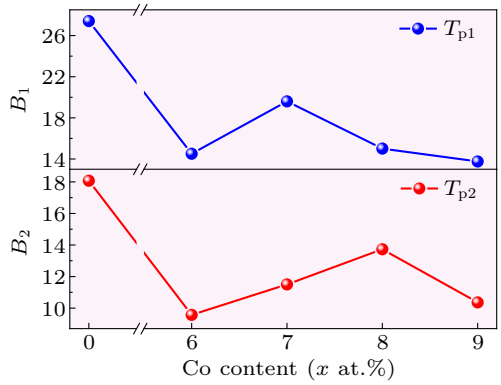


Fig. 7. Variation of B_1 and B_2 values with different Co contents.

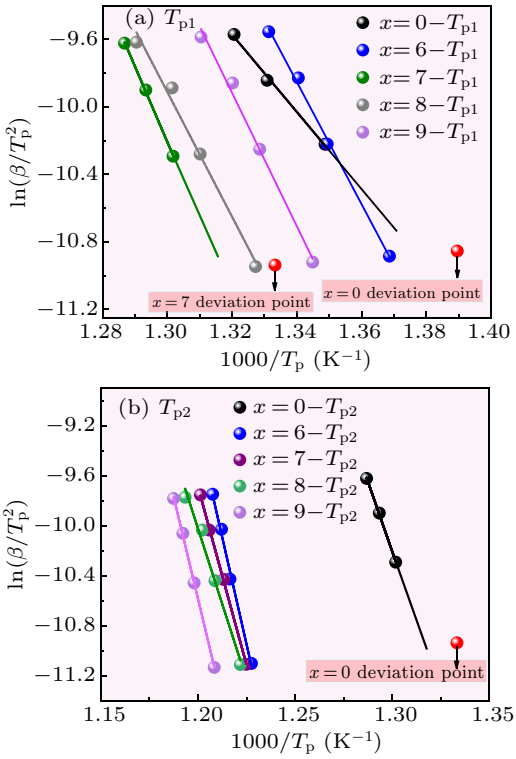


Fig. 8. Kissinger fit diagram of the $(Fe_{40-x}Co_xNi_{40}Si_{6.33}B_{12.66}Cu_1)_{97}Nb_3$ ($x = 0, 6, 7, 8, 9$) as-spun alloy ribbons: (a) T_{p1} and (b) T_{p2}.

Table 1 presents the calculated values of the crystallization activation energy for $(Fe_{40-x}Co_xNi_{40}Si_{6.33}B_{12.66}Cu_1)_{97}Nb_3$ ($x = 0$, 6, 7, 8, 9) alloys. It shows that the activation energies for secondary crystallization (E_{p2}) are higher than those for primary crystallization (E_{p1}) in all alloys, indicating that secondary nucleation is more challenging and requires more energy. As the Co content increases from 0 to 9 at.%, E_{p1} first increases, peaks with $x = 7$, then decreases, and increases again with $x = 9$. The initial increase is likely due to the larger size of γ-(Fe,Ni,Co) clusters, which raises the resistance to crystallization. This larger cluster size requires the atoms to absorb more energy to meet the kinetic conditions necessary for nucleation and growth of the crystalline phase, resulting in a higher E_{p1}. The decrease in E_{p2} may be attributed to the bonding strength and atomic arrangement in the alloy. The atomic bonds of Co and Fe are stronger and arranged more closely, which is conducive to the formation of clusters and reduces the energy required for atomic diffusion. For the $x = 9$, more clusters may increase the activation energy. For E_{p2}, as Co content increases from 0 to 9 at.%, E_{p2} initially increases, peaks with $x = 6$, then decreases, and increases again with $x = 9$. The initial increase is due to fewer nucleation sites, requiring atoms to diffuse longer distances, thus increasing the energy. The subsequent decrease could result from the clustering effect of Co, which provides more nucleation sites and reduces the energy needed for diffusion. For the $x = 9$ alloy, higher Co content may lead to more γ-(Fe,Ni,Co) phase precipitation, reducing Fe content and increasing B proportion, which stabilizes the residual amorphous phase but requires higher temperatures for B diffusion, raising E_{p2}. Thus, adding an appropriate amount of Co improves thermal stability, with the $x = 7$ showing the best stability.

Table 1. Crystallization activation energy of $(Fe_{40-x}Co_xNi_{40}Si_{6.33}B_{12.66}Cu_1)_{97}Nb_3$ ($x = 0, 6, 7, 8, 9$) alloy ribbons.

x (at.%)	E_{p1} (kJ/mol)	E_{p2} (kJ/mol)
0	190.56	372.30
6	300.97	569.01
7	372.30	404.06
8	307.29	398.49
9	328.24	544.48

3.2. Annealing temperature dependence of the magnetic properties

Figures 9(a) and 9(b) show XRD patterns of the alloy ribbons with $x = 0$ and $x = 7$ after annealing in the temperature range of 673 K to 848 K. Figure 9(a) shows that the alloy with $x = 0$ still has an amorphous structure after annealing at 673 K and 698 K. The α-FeNi(Si) main phase is precipitated after annealing at 723 K. After annealing at 848 K, the precipitated phase transforms from α-FeNi(Si) to γ-FeNi(Si). At the same time, a new crystalline phase, the hard magnetic phase (FeNi)B appears. The increase in annealing temperature leads to an increase in the intensity of the diffraction peaks, suggesting that the content of the precipitated phase increases with the increase of temperature. Figure 9(b) shows that the

$x = 7$ alloy exhibits an amorphous structure at annealing temperatures from 673 K to 723 K. After annealing at 748 K, the α-(Fe,Ni,Co) main phase precipitates, and after annealing at 848 K, the precipitated phase partially transforms from α-(Fe,Ni,Co) to γ-(Fe,Ni,Co) with the appearance of $(FeNi)_{23}B_6$. The three different crystalline phases precipitated correspond to the three exothermic peaks of the DSC curves in Fig. 5. In addition, the crystallization temperature of $x = 7$ is higher than that of $x = 0$ alloy. This is consistent with the DSC results, indicating that the addition of Co improves the thermal stability of the alloy. Comparing the XRD patterns of the alloys with $x = 7$ to the standard PDF card of the γ-(FeNi) phase, it was found that the crystal peaks shifted towards higher angles. Co atoms substantially dissolved into the γ-(Fe,Ni,Co) lattices to replace Fe atoms.[28,29] Because the atomic radius of Co is smaller than Fe, causing a distortion of the γ-(Fe,Ni,Co) lattices and a reduce of the lattice parameter a,[30] resulting in the reduce of the crystal plane spacing d, thus leading to the diffraction peaks of γ-(Fe, Ni, Co) shift to higher angles.[16] Figure 9(c) shows the lattice constant a of the $x = 0$ and $x = 7$ alloys annealed at different temperatures. With the annealing temperature increase, the lattice constant a reduces.

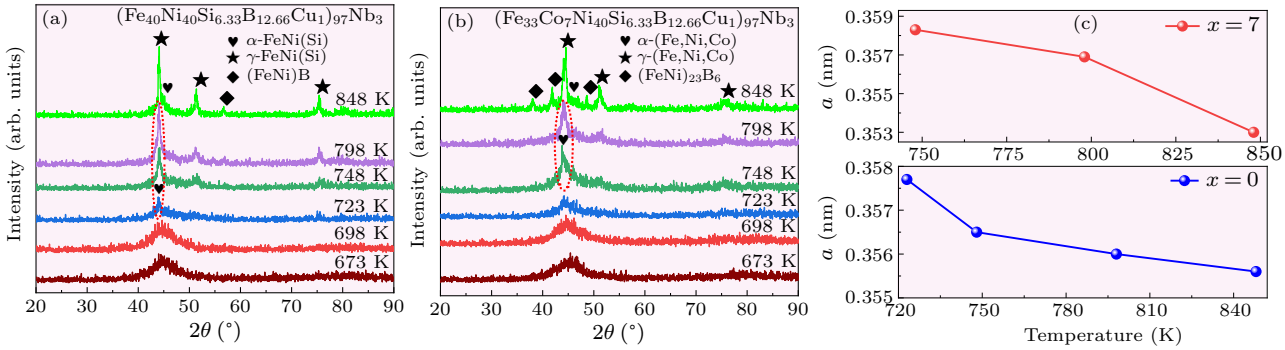


Fig. 9. XRD patterns of $(Fe_{40-x}Co_xNi_{40}Si_{6.33}B_{12.66}Cu_1)_{97}Nb_3$ ($x = 0$, 7) alloy ribbons annealed at different temperatures. (a) $x = 0$, (b) $x = 7$, and (c) lattice constant a of the $x = 0$ and $x = 7$ alloy ribbons annealed at different temperatures.

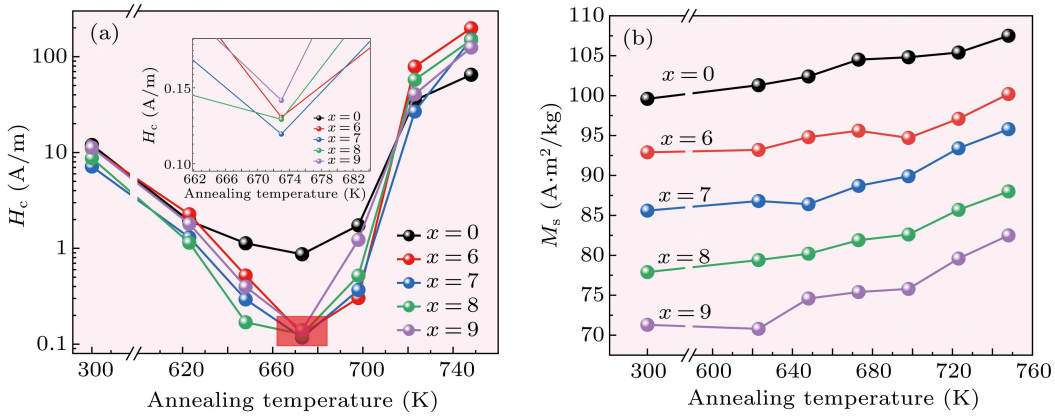


Fig. 10. Variation of (a) H_c and (b) M_s with annealing temperatures of $(Fe_{40-x}Co_xNi_{40}Si_{6.33}B_{12.66}Cu_1)_{97}Nb_3$ ($x = 0$, 6, 7, 8, 9) alloy ribbons.

Figure 10 shows variations of H_c and M_s with annealing temperature for $(Fe_{40-x}Co_xNi_{40}Si_{6.33}B_{12.66}Cu_1)_{0.97}Nb_{0.03}$ ($x = 0$, 6, 7, 8, 9) alloy ribbons. In Fig. 10(a), the H_c of the alloy initially decreases and then increases, reaching a minimum at 673 K. The decrease in H_c is attributed to the annealing process, which eliminates internal stresses, reduces defects, and results in a denser, more uniform structure, thereby diminishing the pinning effect on domain walls. The subsequent increase in H_c is due to the alloy entering a structural relaxation state, which improves magnetic crystal anisotropy. At an annealing temperature of 748 K, the H_c increases significantly due to the formation of crystalline phases and grain growth, which deteriorates the soft magnetic properties. Figure 10(b) shows that the M_s of the alloy exibits an overall increasing trend. The slight increase observed before significant annealing is due to the reduction of internal stress, while the increase observed later is attributed to the precipitation of crystalline phases. Notably, the $(Fe_{33}Co_7Ni_{40}Si_{6.33}B_{12.66}Cu_1)_{0.97}Nb_{0.03}$ alloy shows the best overall magnetic properties after annealing at 673 K, with H_c of 0.12 A/m and M_s of 88.7 A·m^2/kg.

Figure 11 shows the magnetic domain of $(Fe_{33}Co_7Ni_{40}Si_{6.33}B_{12.66}Cu_1)_{97}Nb_3$ ribbons in as-spun state and annealed for 10 minutes at different temperatures. The as-spun magnetic domains are mainly composed of irregular and disordered multi branch magnetic domains and fingerprint like magnetic domains, which are due to the presence of local internal stress, resulting in uneven distribution of magnetic domains and high coercivity.[26] After annealing, the magnetic

domains of the ribbons change from fingerprint like to regular ribbons-shaped, and as the annealing temperature increases, the width of the magnetic domain first increases and then decreases, reaching its maximum value at 673 K. The wider the magnetic domain, the easier it is to flip, the easier the domain wall is to migrate, the smaller the pinning effect on the magnetic domain, and the smaller the coercivity. Therefore, the coercivity of the ribbons first decreases and then increases with the increase of annealing temperature, reaching its minimum value at the annealing temperature of 673 K, which is consistent with the results of the coercivity in Fig. 10(a).

Figure 12(a) shows the effective permeability (μ_e) profiles of $(Fe_{40-x}Co_xNi_{40}Si_{6.33}B_{12.66}Cu_1)_{0.97}Nb_{0.03}$ ($x = 0$, 6, 7, 8, 9) alloy ribbons at various annealing temperatures. As can be seen from Fig. 12(a), the μ_e increases and then decreases with increasing annealing temperature and reaches a maximum at an annealing temperature of 673 K. The μ_e values for the alloys are 10600, 12400, 13800, 10900, and 11400, respectively, with permeability approaching zero after reaching the crystallization temperature. Figure 12(b) shows the μ_e of the alloy under the optimal annealing condition, annealing for 10 min at 673 K. Figure 12(b) shows that, with the addition of Co, μ_e is higher than that of the $x = 0$ alloy in the frequency range of 1 kHz to 10 MHz. Figure 12(c) shows the μ_e varies with the external magnetic field (H_m) at 1 kHz. As H_m increases from 1 A/m to 60 A/m, μ_e first increases and then decreases. The maximum μ_e corresponds to the pinning field (H_p) of the alloys. A smaller pinning field shows fewer pinning points and defects in the alloys. The results show that the alloy with $x = 7$ has the lowest H_p of 20 A/m, suggesting superior soft magnetic properties.

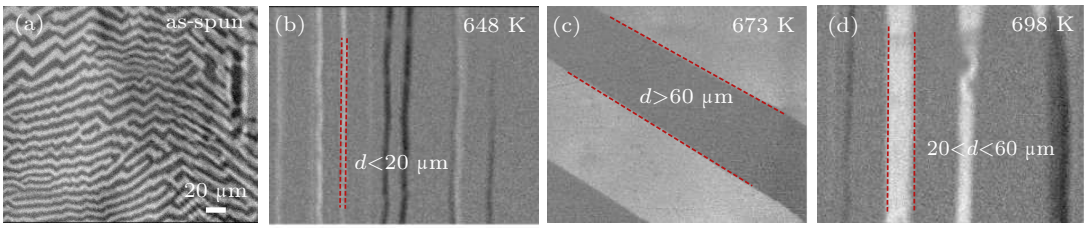


Fig. 11. Magnetic domain of $(Fe_{33}Co_7Ni_{40}Si_{6.33}B_{12.66}Cu_1)_{97}Nb_3$ ribbons (a) as-spun and annealed at different temperatures for 10 min, (b) 648 K, (c) 673 K, and (d) 698 K.

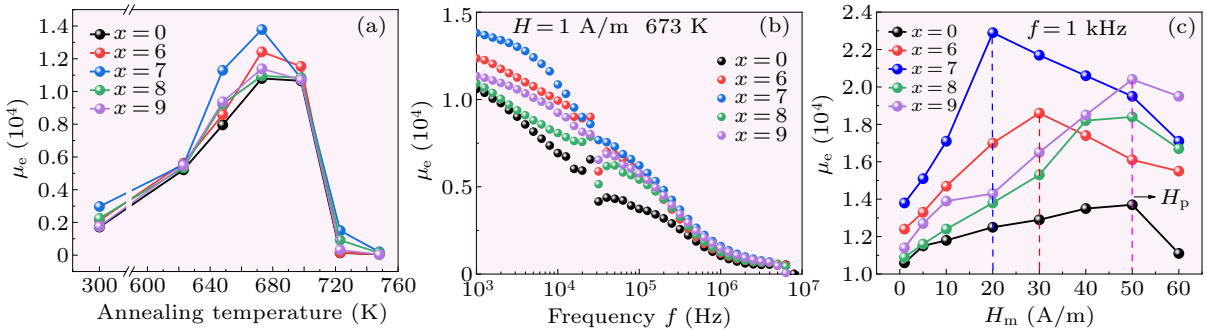


Fig. 12. (a) Effective permeability (μ_e) of $(Fe_{40-x}Co_xNi_{40}Si_{6.33}B_{12.66}Cu_1)_{97}Nb_3$ ($x = 0$, 6, 7, 8, 9) ribbons annealed at different temperatures, (b) the μ_e of $x = 0$, 6, 7, 8, 9 at.% ribbons annealed at 673 K and (c) the change of μ_e with H_m at 1 kHz of $x = 0$, 6, 7, 8, 9 ribbons.

Table 2. Coercivity comparison of FeNi-based amorphous alloys.

Alloy	H_c (A/m)
$(Fe_{33}Co_7Ni_{40}Si_{6.33}B_{12.66}Cu_1)_{97}Nb_3$ (the study)	0.12
$Fe_{39}Ni_{39}B_{12.82}Si_{2.75}Nb_{2.3}P_{4.13}$ [a]	0.65
$(Ni_{0.5}Fe_{0.3}Co_{0.2})_{80}B_{10}Si_2Cu_1Zr_7$ [b]	5
$Fe_{80}Ni_5Si_2B_8P_4Cu_1$ [c]	14.3
$(Fe_{40}Ni_{40}Si_{6.4}B_{12.6}Cu_1)_{0.97}Nb_{0.03}$ [d]	0.25
$Fe_{40}Ni_{38}Mo_4B_{18}$ [e]	0.94
$(Fe_{70}Ni_{30})_{85}Nb_{0.5}B_{14.5}$ [f]	17

[a]Ref. [1], [b]Ref. [16], [c]Ref. [27], [d]Ref. [32], [e]Ref. [33], [f]Ref. [34].

To further investigate the impact of annealing times on the soft magnetic properties of amorphous alloys, the $(Fe_{33}Co_7Ni_{40}Si_{6.33}B_{12.66}Cu_1)_{97}Nb_3$ alloy was annealed at 673 K for 3 min, 10 min, and 20 min. Figure 13(a) shows the XRD patterns of the $(Fe_{33}Co_7Ni_{40}Si_{6.33}B_{12.66}Cu_1)_{97}Nb_3$ alloy ribbons annealed at 673 K for different time. It shows that XRD patterns remain scattering peaks after annealing, indicating that the alloy remains amorphous structure. Figure 13(b) presents the variation of M_s and H_c with annealing time, compared to the as-spun alloy, the M_s initially increases and then decreases with annealing time, peaking at 10 min. The initial increase is attributed to reduced residual stress and excess free volume after annealing, which reduces structural distortion and improves magnetic exchange interactions.[31] However, the change is modest because M_s is relatively insensitive to structural changes, being more influenced by phase composition and alloy constituents. The H_c initially decreases and then increases, reaching its minimum at 10 min. As an-

nealing progresses, residual stress is gradually eliminated. At 10 min, residual stress is nearly fully removed, resulting in the lowest H_c. Prolonged annealing causes atomic diffusion and compositional inhomogeneity, increasing magnetic anisotropy and coercivity. Thus, at an annealing temperature of 673 K for 10 min, the alloy shows optimal magnetic properties, with $H_c = 0.12$ A/m and $M_s = 88.7$ A·m^2/kg. Table 2 compares research advancement in FeNi-based amorphous alloys, showing that the $(Fe_{33}Co_7Ni_{40}Si_{6.33}B_{12.66}Cu_1)_{97}Nb_3$ alloy in this study has low coercivity.

Figure 14 shows the magnetic domains of alloys $(Fe_{33}Co_7Ni_{40}Si_{6.33}B_{12.66}Cu_1)_{97}Nb_3$ annealed at 673 K for different time. It can be seen that the width of the magnetic domains increases and then decreases with the increase of annealing time, and reaches the maximum when the annealing time is 10 min. It coincides with the variation trend of coercivity in Fig. 13(b).

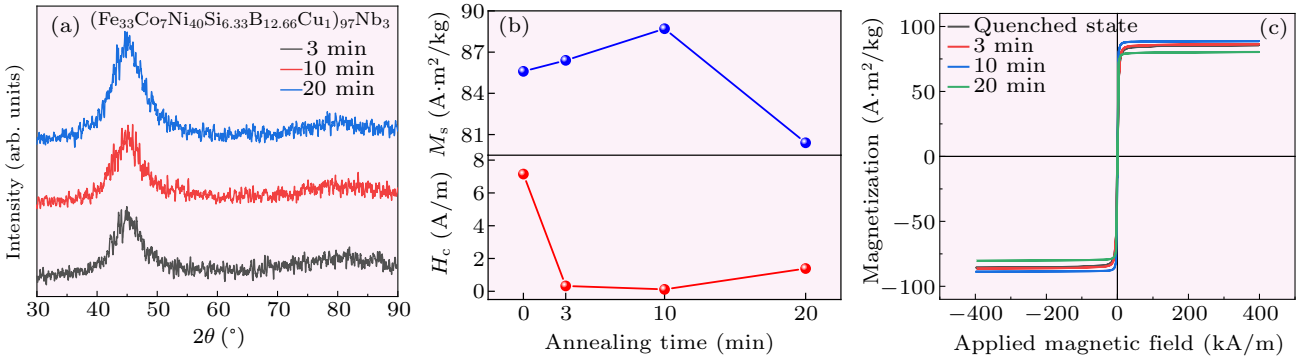


Fig. 13. (a) XRD patterns, (b) variations of M_s and H_c with annealing time and (c) magnetic hysteresis loop of $(Fe_{33}Co_7Ni_{40}Si_{6.33}B_{12.66}Cu_1)_{97}Nb_3$ ribbon annealed at 673 K for different time.

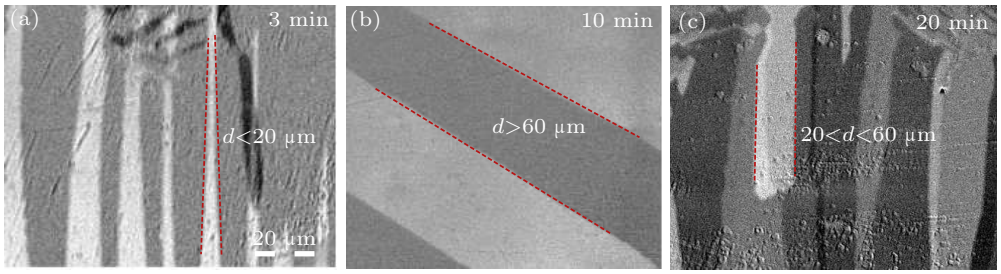


Fig. 14. Magnetic domains of $(Fe_{33}Co_7Ni_{40}Si_{6.33}B_{12.66}Cu_1)_{97}Nb_3$ ribbons annealed at 673 K for different time: (a) 3 min, (b) 10 min, and (c) 20 min.

4. Conclusion

In this paper, we investigated the influences of the substitution of Fe by Co on the glass formation ability (GFA), thermal stability, and soft magnetic properties of $(Fe_{40-x}Co_xNi_{40}Si_{6.33}B_{12.66}Cu_1)_{97}Nb_3$ alloys ($x = 0$, 6, 7, 8, 9). It also explores the effects of annealing on these properties and analyzes the alloys crystallization kinetics. The conclusions are as follows:

(i) Partial substitution of Co for Fe effectively improves the GFA of $(Fe_{40-x}Co_xNi_{40}Si_{6.33}B_{12.66}Cu_1)_{97}Nb_3$ ($x = 0$, 6, 7, 8, 9) alloys.

(ii) With the addition of Co element, the E_{p1} increased, indicating that the thermal stability is improved. For $x = 7$, E_{p1} reaches a maximum of 372.3 kJ/mol, and the ΔT_x is maximized of 90, showing the best thermal stability.

(iii) The $(Fe_{33}Co_7Ni_{40}Si_{6.33}B_{12.66}Cu_1)_{97}Nb_3$ alloy shows the best overall soft magnetic properties after annealing at 673 K for 10 min, with coercivity $H_c = 0.12$ A/m, saturated magnetization $M_s = 88.7$A·m^2/kg, and effective permeability $\mu_e = 13800$. And annealing removes numerous pinning points in the magnetic domains of the alloy ribbons, making the domain walls smoother and effectively reducing the pinning effect.

Acknowledgements

Project supported by the National Natural Science Foundation of China (Grant No. 52275567), the Key Research and Development Program of Shanxi Province, China (Grant No. 202202050201020), the Doctoral Starting-up Foundation of Taiyuan University of Science and Technology (Grant No. 20192016), the Research Project Supported by Shanxi Scholarship Council (Grant No. 2017-085), the Graduate Education and Teaching Reform Project of Shanxi Province, China (Grant No. 2023JG136), and the Special Fund for Science and Technology Innovation Teams of Shanxi Province, China (Grant No. 202304051001036).

References

[1] Hasegawa R 2004 *Mater. Sci. Eng. A* **375–377** 90

[2] Jia X J, Li Y H, Wu L C and Zhang W 2020 *J. Alloys Compd.* **822** 152784
[3] Huo J T, Li K Y, Zang B W, Gao M, Wang L M, Sun B A, Li M Z, Song L J, Wang J Q and Wang W H 2022 *Chin. Phys. Lett.* **39** 046401
[4] Wang A D, Zhao C L, He A N, Yue S Q, Chang C T, Shen B L, Wang X M and Li R W 2016 *Intermetallics* **71** 1
[5] Pang J, Qiu K Q, Kong F Y, Wang A D, Liang X F, Wang C J, Chang C T, Wang X M and Liu C T 2017 *J. Non-Cryst. Solids* **471** 238
[6] Xiao J H, Ding D W, Li Lin, Sun Y T, Li M Z and Wang W H 2024 *Chin. Phys. B* **33** 076101
[7] Zhou J, Wang Q Q, Hui X D, Zeng Q S, Xiong Y W, Yin K B, Sun B A, Sun L T, Stoica M H, Wang W H and Shen B L 2020 *Mater. Des.* **191** 108597
[8] Chen Z, Zhu Q K, Zhang K W, Guo Q and Jiang Y 2020 *J. Mater. Sci.* **56** 4871
[9] Raya I, Chupradit S, Kadhim M M, Mahmoud M, Jalil A T, Surendar A, Ghafel S T, Mustafa Y F and Bochvar A N 2022 *Chin. Phys. B* **31** 016401
[10] Huang H, Tsukahara H, Kato A, Ono K and Suzuki K 2024 *J. Magn. Magn. Mater.* **592** 171810
[11] Yu W Q, Tian B, Zhang P L, Wang J H and Hua Z 2023 *Chin. Phys. B* **32** 088102
[12] Hao Z Y, Wei L Z, Wang Y C, Kawazoe Y, Liang X Y, Umetsu R, Yodoshi N, Tong X, Xia W X, Zhang Y and Cao C D 2022 *J. Alloys Compd.* **920** 166029
[13] Kostyrya S A and Idzikowski B 2006 *J. Magn. Magn. Mater.* **304** e537
[14] Liang Y C, Xian G, Zhou L L, Tian Z A, Chen Q, Mo Y F, Liu R S, Gao T H, Xie Q and He M 2022 *J. Alloys Compd.* **891** 161953
[15] Gheiratmand T and Hosseini H R M 2016 *J. Magn. Magn. Mater.* **408** 177
[16] Sheng W W, Qiu Z G, Zheng Z G, Liu X and Zeng D C 2021 *J. Non-Cryst. Solids* **559** 120677
[17] Sheng W W, Qiu Z G, Zheng Z G and Zeng D C 2021 *J. Alloys Compd.* **855** 157436
[18] Zhang Y, Sharma P and Makino A 2014 *IEEE Trans. Magn.* **50** 2006804
[19] Tong X, Zhang Y, Wang Y C, Liang X Y, Zhang K, Zhang F, Cai Y F, Ke H B, Wang G, Shen J, Makino A and Wang W H 2022 *J. Mater. Sci. Technol.* **96** 233
[20] Xi G G, Sun C, Han M H, Li H G, Cui J L and Zhang T 2024 *J. Non-Cryst. Solids* **633** 122951
[21] Li M X, Sun Y T, Wang C, Hu L W, Sohn S, Schroers J, Wang W H and Liu Y H 2022 *Nat. Mater.* **21** 165
[22] Song K K, Bian X F, Guo J, Li X L, Xie M T and Dong C J 2008 *J. Alloys Compd.* **465** L7
[23] Michalski P P, Pietrzak T K, Nowiński J L, Wasiucionek M and Garbarczyk J E 2016 *J. Non-Cryst. Solids* **443** 155
[24] Chen Z, Zhu Q K, Zhang K W and Jiang Y 2020 *Cryst. Growth Des.* **20** 2187
[25] Zhao M, Yang D, Zhang W, Liu H Y, Xiang Q C, Pang J, Ren Y L, Li X Y and Qiu K Q 2024 *J. Alloys Compd.* **988** 174267
[26] Wang Y F, Xu J, Liu Y J and Liu Z W 2022 *Mater. Charact.* **187** 111830
[27] Farjas J and Roura P 2014 *Thermochimica Acta* **598** 51
[28] Zhang Y, Zhou Y J, Lin J P, Chen G L and Liaw P K 2008 *Adv. Eng. Mater.* **10** 534
[29] Zuo T T, Zhang M, P Liaw K and Zhang Y 2018 *Intermetallics* **100** 1
[30] Zou J H, Gao R L, Fu C L, Cai W, Chen G and Deng X L 2018 *Process. Appl. Ceram.* **12** 335
[31] Chen Z, Zhu Q K, Zhang K W, Guo Q and Jiang Y 2021 *J. Mater. Sci.* **56** 4871
[32] Jia X J, Li Y H, Wu L C and Zhang W 2020 *J. Alloys Compd.* **822** 152784
[33] Zhu Q K, Guo L, Chen Z, Jiang Y, Li M, Zhang K W, Hu J F, Li W and Guo Q 2022 *J. Non-Cryst. Solids* **593** 121776
[34] Talaat A, Egbu J, Phatak C, Byerly K, McHenry M E and Ohodnicki P R 2022 *Mater. Res. Bull.* **152** 111839